ISSN 1062-8738, Bulletin of the Russian Academy of Sciences: Physics, 2023, Vol. 87, Suppl. 1, pp. S133–S146. © Pleiades Publishing, Ltd., 2023.

Ferromagnetic Silicides and Germanides Epitaxial Films and Multilayered Hybrid Structures: Synthesis, Magnetic and Transport Properties

A. S. Tarasov[a, b, *] (ORCID: 0000-0001-8187-1550), A. V. Lukyanenko[a, b] (ORCID: 0000-0001-7496-242X), I. A. Yakovlev[a] (ORCID: 0000-0001-5988-2835), I. A. Tarasov[a] (ORCID: 0000-0002-2113-9234), I. A. Bondarev[a, c] (ORCID: 0000-0001-8155-3958), A. L. Sukhachev[a] (ORCID: 0000-0003-4644-8823), L. V. Shanidze[a] (ORCID: 0000-0002-5614-9010), D. A. Smolyakov[a] (ORCID: 0000-0002-3953-9770), S. N. Varnakov[a] (ORCID: 0000-0003-2676-2460), S. G. Ovchinnikov[a, b] (ORCID: 0000-0003-1209-545X), and N. V. Volkov[a]

[a] *Kirensky Institute of Physics, Federal Research Center "Krasnoyarsk Scientific Center," Siberian Branch, Russian Academy of Sciences, Krasnoyarsk, 660036 Russia*

[b] *Institute of Engineering Physics and Radio Electronics, Siberian Federal University, Krasnoyarsk, 660041 Russia*

[c] *Federal Research Center "Krasnoyarsk Scientific Center," Siberian Branch, Russian Academy of Sciences, Krasnoyarsk, 660036 Russia*

**e-mail: taras@iph.krasn.ru*

Received September 29, 2023; revised October 3, 2023; accepted October 9, 2023

Abstract—Planar and vertical hybrid structures, which combine ferromagnetic and semiconductor layers are essential for implementation and study of spin transport phenomena in semiconductors, which is crucial for the advancement and development of spintronics. We have developed approaches for the synthesis of $Fe_{3+x}Si_{1-x}$ epitaxial thin films and demonstrated the spin accumulation effect in multiterminal devices based on $Fe_{3+x}Si_{1-x}$/Si. $Fe_{3+x}Si_{1-x}$/Ge/Fe_3Si and $Fe_{3+x}Si_{1-x}$/Ge/Mn_5Ge_3 multilayer hybrid structures were synthesized on a Si(111) substrate, study of their structural, magnetic and transport properties were performed. The effect of synthesis conditions on the growth of epitaxial structures and on their magnetic and transport properties was discussed. The results obtained may prove valuable in the development and fabrication of spintronic devices.

Keywords: iron silicide, manganese germanide, MBE, FMR, electronic transport, spintronics

DOI: 10.1134/S1062873823704518

INTRODUCTION

The ongoing challenge of the miniaturization of field-effect transistors (MOSFETs), which is nearing its limits, can be overcome by switching to spintronic devices, which principle of operation is based on the spin degrees of freedom, offering the potential to reduce overall power consumption, improve the speed of RAM and expand the capabilities of data processing [1–5]. The search for suitable ferromagnetic (FM) materials for spintronic devices is a complex and urgent task, since such materials must be compatible with the silicon technology, which is currently dominant in the semiconductor (SC) industry, have a high transition temperature to the FM state (T_C) and high spin polarization of electrons, and meet a number of other requirements as well. Such materials include many Heusler alloys [6–13], for example Fe_2MnSi, Fe_3Si, Co_2FeAl, Co_2FeSi, $Co_2Fe(Al,Si)$. Based on such ferromagnets, both simple FM/SC epitaxial structures and multilayer hybrid structures of various compositions can be grown. Of particular interest are three-layer FM/SC/FM hybrid structures are promising for vertical and planar devices of semiconductor spintronics [14–17]. Electrical response from hybrid structures can be easily controlled and tuned by external influences like temperature, electrical bias, magnetic field [18, 19], optical irradiation [20, 21] and other. We have developed approaches for the synthesis of $Fe_{3+x}Si_{1-x}$ epitaxial thin films and demonstrated the spin accumulation effect in multiterminal devices based on $Fe_{3+x}Si_{1-x}$/Si. $Fe_{3+x}Si_{1-x}$/Ge/Fe_3Si and $Fe_{3+x}Si_{1-x}$/Ge/Mn_5Ge_3 multilayer hybrid structures were synthesized on a Si(111) substrate, studies of their structural, magnetic and transport properties were performed.

SAMPLE SYNTHESIS AND EXPERIMENTAL DETAILS

All film samples were grown on Si(111) substrates by molecular beam epitaxy at a base vacuum of 6×10^{-8} Pa. Before loading into an ultrahigh vacuum (UHV) chamber, a chemical treatment in air was performed using a H_2O_2 : NH_4OH : H_2O solution in the ratio 1 : 1 : 1 and a 5% hydrofluoric acid solution (HF). Immediately prior to the deposition of specific materials, the Si(111) substrates were annealed at a temperature of 900°C to obtain a 7×7 surface reconstruction, which was monitored in situ using reflected high-energy electron diffraction (RHEED). Details about the stages of substrate preparation are described in [22]. Individual materials (Fe, Si, Ge, Mn) were evaporated from separate sources at different rates to provide the required stoichiometry of binary compounds. The deposition rates of individual materials were previously calibrated by laser ellipsometry. Knudsen cells with indirect thermal heating of the crucible were used as sources. The deposition of $Fe_{3+x}Si_{1-x}$ iron silicide layers was carried out using co-deposition from different sources of iron and silicon in an atomic ratio of 3 : 1. The ratio of deposition rates Si : Fe ≈ 0.57 is stoichiometric for Fe_3Si. The fabrication of iron silicides is a well-established technology, and the details of the epitaxial synthesis of iron silicide with the DO3 structure were described in [22, 23]. During the growth of $Fe_{3+x}Si_{1-x}$ films, the substrate temperature was stabilized for 30 min and was maintained at 150°C, for Ge at 300°C, and for Mn_5Ge_3 at 390°C. The parameters of the epitaxial films were controlled in situ using an LEF 751M laser ellipsometer and RHEED. In total, 4 types of samples were synthesized: single-layer thin films Fe_3Si and Mn_5Ge_3 as well as multilayer structures $Fe_{3+x}Si_{1-x}$/Ge/Fe_3Si and $Fe_{3+x}Si_{1-x}$/Ge/Mn_5Ge_3.

Based on the obtained samples, multiterminal structures of a special topology were prepared using standard optical lithography and wet chemical etching. On the surface of the $Fe_{3+x}Si_{1-x}$, film, a protective mask was formed using photolithography, so the area of the film covered with photoresist was protected from the acid solution, and the rest of the film was removed using a solution of hydrofluoric (HF) and nitric (HNO_3) acids in water (H_2O) with a component ratio of 1 : 2 : 400, which provided an etching rate of ~52 Å/s for the stoichiometric composition of Fe_3Si iron silicide. Details on fabrication and features of the chemical etching process are described in [23].

The microstructure of the samples was studied using atomic force microscopy (AFM) and transmission electron (TEM) microscopy. X-ray diffraction (XRD) analysis was done using PANalytical X'Pert PRO diffractometer equipped with a solid-state detector PIXcel using CuK_α radiation. The film surface morphology was measured using AFM in the semicontact scanning mode (DPN 5000, NanoInk, USA) using probes with a curvature radius of ~6 nm (CSG30, NT-MDT SI, Russia). AFM data processing and image statistical analysis were performed using the free software Gwyddion (version 2.51). Cross-section TEM images of the films were obtained using a focused ion beam (FIB) FB-2100 (Hitachi, Japan) setup for electron microscopy studies. Static and dynamic magnetic properties were studied using the equipment of the Krasnoyarsk Regional Center of Research Equipment of Federal Research Center "Krasnoyarsk Science Center, Siberian Branch, Russian Academy of Sciences" Lakeshore's 8600 Series vibration sample magnetometer (VSM) and Bruker's ELEXSYS-E580 electron paramagnetic resonance (EPR) spectrometer. The electrical resistance and I–V curves were measured using a precision multimeter Keithley 2634b SourceMeter in the temperature range from 4.2 to 300 K provided by a helium flow cryostat on homebuilt facility [24].

STRUCTURAL PROPERTIES STUDY WITH RHEED, TEM AND AFM

Single-layer epitaxial $Fe_{3+x}Si_{1-x}$ iron silicide films were studied in detail by transmission electron microscopy (TEM) (Fig. 1a) and atomic force microscopy (AFM) [23]. Based on the final RHEED picture (Fig. 1b) one can conclude that the $Fe_{3+x}Si_{1-x}$ layer on Si(111)7×7 was formed epitaxially and has a single-crystal structure. Figure 1a shows typical TEM images along the [110] axis for $Fe_{3+x}Si_{1-x}$. It can be seen that the films are homogeneous and do not contain grains of different orientations; the film surface roughness is about ~2 nm. Furthermore, a clear and smooth interface between the film and the substrate is observed, without a diffusion layer. A typical AFM surface morphology image is shown in Fig. 1c. AFM topographic data show a small number of surface defects. The root means square roughness (Sq) parameter representing graininess is 0.86 nm. Rms (Rq) value is 0.51 nm. The surface roughness (Sa) is 1.13 nm, which is consistent with the TEM results.

Three-layer hybrid structures $Fe_{3+x}Si_{1-x}$/Ge/Fe_3Si/Si(111) (Fig. 2a) with different germanium thicknesses (4 and 7 nm) were synthesized by sequential deposition of iron and germanium silicide layers. The entire synthesis process was controlled in situ using RHEED. It can be seen from the diffraction data (Figs. 2b, 2e) that the first Fe_3Si layer on Si(111)7×7 has a single crystal structure. After obtaining the first layer of silicide, the temperature of the sample was increased to 300°C, and after its stabilization, a layer of germanium was deposited (4 and 7 nm, respectively, we will designate them as #Ge4 and #Ge7). Figures 2c, 2f shows the RHEED data for the second layer and it can be seen that the germanium layer also has an epitaxial, single crystal structure. For sample #Ge7, the RHEED pattern for the germanium layer is slightly

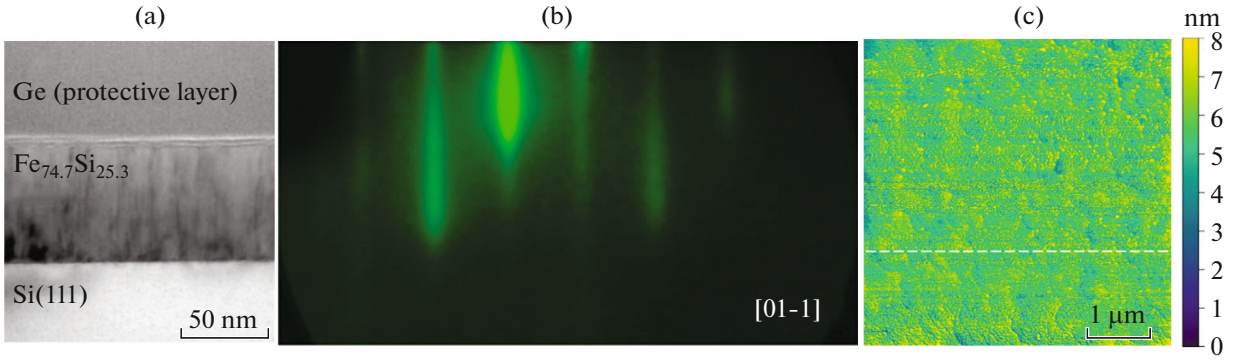

Fig. 1. (a) TEM, (b) RHEED and (c) AFM data for Fe_3Si/Si(111). The Rms (Rq) data are taken along the white dotted line.

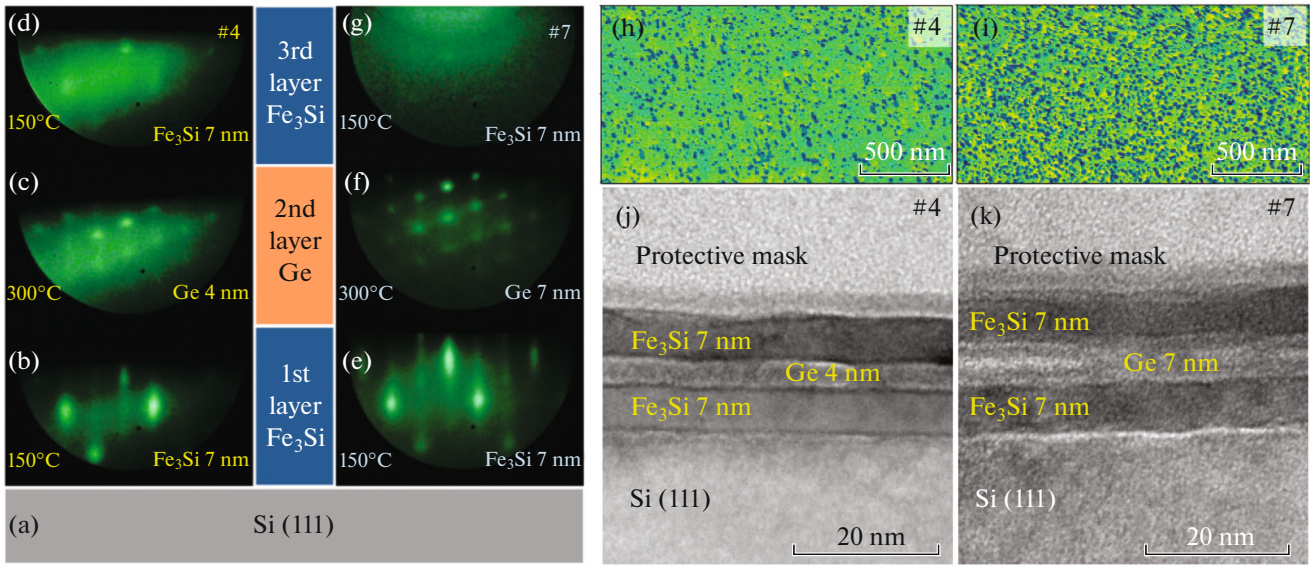

Fig. 2. RHEED (a–e), TEM (j–k) and 1 × 2 μm^2 AFM (h–i) (pseudo color bar range from 0 to 10 nm) for $Fe_{3+x}Si_{1-x}$/Ge (4 nm)/Fe_3Si/Si(111) and $Fe_{3+x}Si_{1-x}$/Ge (7 nm)/Fe_3Si/Si(111).

more pronounced, compared to the thinner layer on #Ge4 sample. The third layer of the hybrid structure, like the first one, consists of iron silicide and was obtained under the same technological conditions. The top layer of silicide formed better on a sample with a thin germanium layer. The corresponding RHEED pictures are shown in Figs. 2d, 2g. The RHEED pattern for #Ge4 shows reflections in the form of dots repeating the geometry of the diffractogram from the first layer (Fig. 2d). However, for #Ge7, only reflections in the form of Debye rings are present (Fig. 2g). This geometry of the diffractogram indicates the formation of a nanocrystalline or polycrystalline structure of the film. These initial analytical results were obtained directly in the UHV chamber, after which more detailed studies were undertaken using AFM and TEM, which are in unambiguous agreement with the RHEED data. From TEM images (Figs. 2j and 2k) we can see three distinct layers lying between Si(111) and the protective layer. During this experiment, the thicknesses of the grown layers were refined (as noted in the figure), which was 7 nm for the Fe_3Si layers for both #Ge4 and #Ge7 samples.

Figures 2h, 2i show typical AFM images of the #Ge4 and #Ge7 surface topology. When scanning a 2 × 2 μm^2 area, one can distinguish nanoscale depressions on the surface of the iron silicide film. The density of depressions is different for #Ge4 and #Ge7, which is confirmed by the statistics. Thus, for the #Ge4 sample, the depressions are 17.3%, and for the #Ge7 sample—43.1% of the projection area. RMS roughness parameter Sq(#Ge4) = 1.5 nm. The surface roughness Sa(#Ge4) = 1.1 nm. Rms(Rq) for #Ge4 is 0.97 nm. Parameters Sq(#Ge7) = 2.2 nm; Sa(#Ge7) = 1.9 nm; Rms(Rq) for #Ge7 is 1.5 nm. A significant difference in the structures' surface morphology indicates different formation mechanisms for the

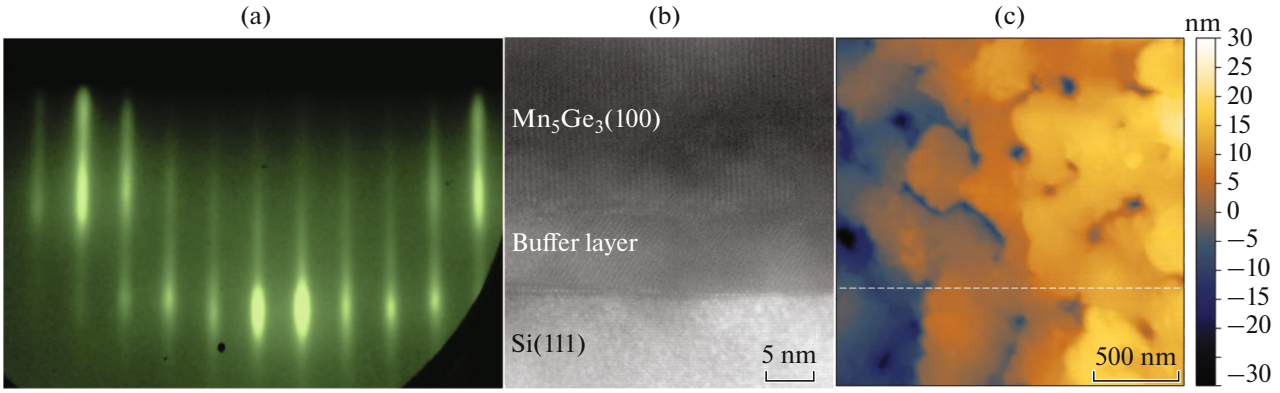

Fig. 3. RHEED (a) TEM (b) and AFM (c) $2 \times 2\ \mu m^2$ (pseudo color scale range from −30 to 30 nm) for Mn_5Ge_3 epitaxial film.

samples. Variation of the thermal history of the samples results in different levels of Ge atoms incorporation into $Fe_{3+x}Si_{1-x}$ layers and causes variation of residual stress [25].

Single-layer epitaxial Mn_5Ge_3 films were synthesized on Si(111). Earlier, the successful synthesis of Mn_5Ge_3 films on Si substrates has not been reported, which is most likely due to a rather large lattice mismatch (8%). By reducing the amount of manganese in the composition, it was possible to reduce this mismatch and grow a buffer layer depleted of manganese with a smooth transition to a stoichiometric ratio of 5 : 3. As a result of optimizing the synthesis temperature and the composition of the buffer layer, it was possible to achieve a stable growth of Mn_5Ge_3 with a thickness of 165 nm on Si(111). Throughout the growth process, reflexes in the form of vertical lines remained in the RHEED pattern. Reflexes are clearly observed in the final RHEED picture presented in Fig. 3a which is an indicator of the formation of only an epitaxial film up to the cessation of synthesis.

The RHEED and XRD data (not shown here) suggest an epitaxial growth regime. In addition to RHEED, AFM measurements were performed. As can be seen from Fig. 3 RHEED and AFM correlate well with each other, which is expected since both methods are surface sensitive. AFM image presented in Fig. 3c shows a typical surface with clearly visible terraces of uneven lengths, with the morphology as in [26] where Mn_5Ge_3 thin films were grown on Ge(111) substrates. An analysis of $2 \times 2\ \mu m^2$ scans AFM statistics shows that the RMS roughness (Sq) is rather low (3.2 nm) which indicates the coalescence of 3D islands at the initial stages of growth. The RMS (Rq) parameter ranges from 0.08 to 0.31 nm, and for the section marked with a white dotted line (Fig. 3c) is 0.09 nm. This clearly indicates a high surface homogeneity and the absence of large peculiarities. For example, the RMS parameter for films in [26] is 0.76 nm. The evolution of the RHEED intensity during deposition and the AFM data show that a step-flow growth mode is likely to occur. TEM image of the obtained Mn_5Ge_3 film is presented in Fig. 3b. The cross-sectional image demonstrates a sharp interface between Mn_5Ge_3 and the buffer layer with a slope of 55.49 degrees relative to the Si(111) substrate.

Three-layer hybrid structures $Fe_{3+x}Si_{1-x}$/Ge/Mn_5Ge_3/Si(111) were synthesized by combining the growth technology of three-layer silicide-based structures and the obtained information about the features of Mn_5Ge_3 growth. Figures 4a–4d shows pictures of RHEED taken during the structure growth. For the Mn_5Ge_3 film, epitaxy is clearly observed, as confirmed by long strikes on Fig. 4b. In the picture, reflections in the form of dots appear from a thin Ge layer (Fig. 4c), which may be indicative of the presence of non-continuous film regions. For the upper $Fe_{3+x}Si_{1-x}$ layer, the RHEED pattern is more typical for transmission diffraction (Fig. 4d), which clearly indicates a columnar microstructure of the film. Most likely, Ge and $Fe_{3+x}Si_{1-x}$ films are textured. The total thicknesses for the films are about 100 nm for Mn_5Ge_3, 7 nm for Ge, and 50 nm for $Fe_{3+x}Si_{1-x}$.

MAGNETIC AND TRANSPORT PROPERTIES

1. $Fe_{3+x}Si_{1-x}$/Si(111)

Using ferromagnetic resonance (FMR) technique the presence of magnetic crystal anisotropy in epitaxial $Fe_{3+x}Si_{1-x}$ thin films was established. Figure 5 shows the experimental and calculated azimuthal angular dependences of the FMR resonance field in polar coordinates. Based on the FMR data, the following parameters were calculated: saturation magnetization M_s = 995 G, uniaxial magnetic anisotropy field F_{ua} = 2.7 Oe, magnetic cubic anisotropy field F_c = 0.9 Oe, film mosaicity parameter $\Delta\theta$ = 0.15, which is indicative of the high quality of the film. The saturation magnetization of the Fe_3Si film is larger than that of similar films obtained on Si(111) (M_s = 800 G) [27] and GaAs(100) (M_s = 790 G) [28] sub-

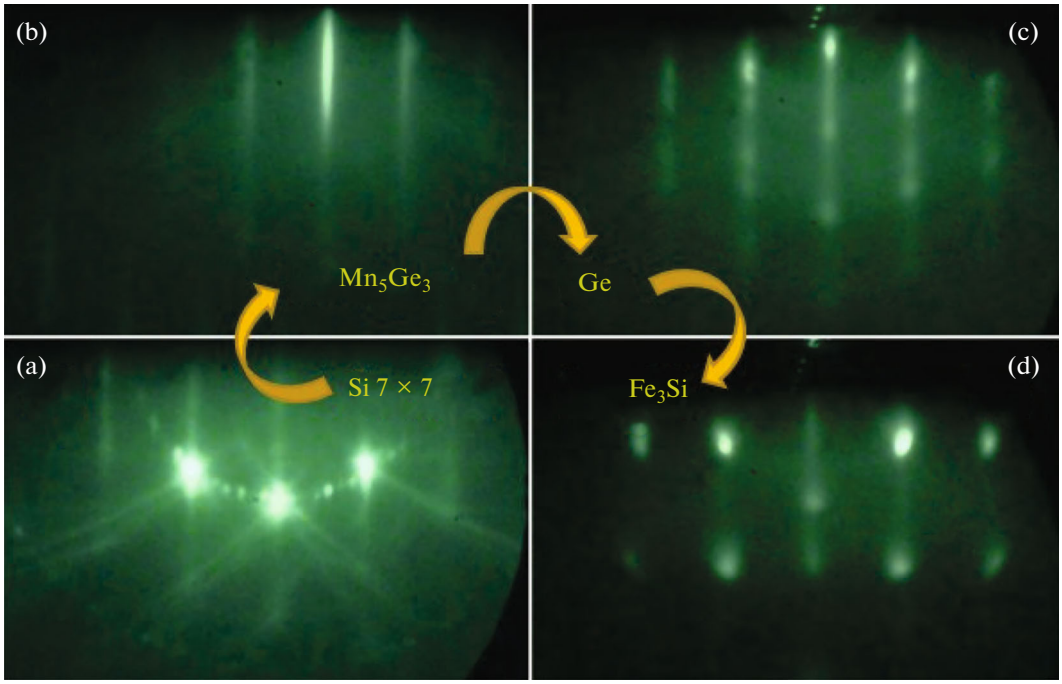

Fig. 4. RHEED patterns for surfaces of (a) Si, (b) Mn_5Ge_3, (c) Ge and (d) Fe_3Si layer.

strates, and also very close to the saturation magnetization of the Fe_3Si, film obtained on a single-crystal MgO(100) substrate (M_s ~ 1000 G) [29]. The small field values of magnetic uniaxial and unidirectional anisotropy are indicative of a high magnetic homogeneity of the sample. However, the small field of magnetic cubic anisotropy can be caused by the mosaic nature of the sample. The absolute value of the linewidth of the FMR spectrum can also serve as an additional parameter of film homogeneity. Thus, when the magnetic field is oriented along the plane of the film, ΔH_{pp} is 18 Oe, which is only 1 Oe more than for the $Fe_{3+x}Si_{1-x}$ film grown on GaAs(100) [28].

Further, using the $Fe_{3+x}Si_{1-x}/p(n)$-Si, hybrid structures selected in the course of complex characterization, Schottky diodes and multiterminal planar devices were fabricated using lithography and liquid etching. The impurity concentration for the substrates was the same ($p(n) = 2 \times 10^{15}$ cm^{-3}) in order to compare the results of electron and hole spin-dependent transport. For Fe_3Si/p-Si structures, systematic studies of spin-dependent electron transport were carried out using the three-terminal Hanle technique in a wide temperature range (Fig. 6a). The calculated values of the spin lifetime τ (145 ps at 300 K) are in good agreement with other experimental data for silicon measured by the 3-terminal technique. For example, for a structure with an epitaxial MgO(001) tunnel barrier layer and an Fe(001) electrode, the lifetime in highly doped p-Si is 133 ps at an injection current of 0.85 mA [30]. In [31] there are the lifetime values in highly doped p-Si with an Al_2O_3 tunnel barrier for various ferromagnetic electrodes, which are 60, 110, and 270 ps for Fe, Co, and $Ni_{80}Fe_{20}$ electrodes, respectively. The value of 470 ps is given in [32] for the M/SC structure Fe_3Si/n-Si with a Schottky tunnel barrier. It is important to note that our Fe_3Si/p-Si structure does not have an insulating layer between the ferromagnet and the semiconductor, and silicon has a rather high resistivity (8 Ohm cm), which, according to the standard theory of spin diffusion [33] should strongly sup-

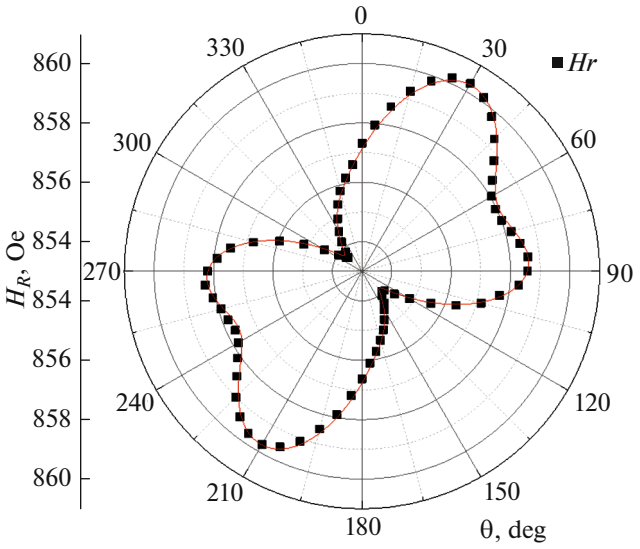

Fig. 5. Experimental (symbols) and calculated (line) azimuthal dependences of FMR resonance field for $Fe_{3+x}Si_{1-x}$/Si(111) sample.

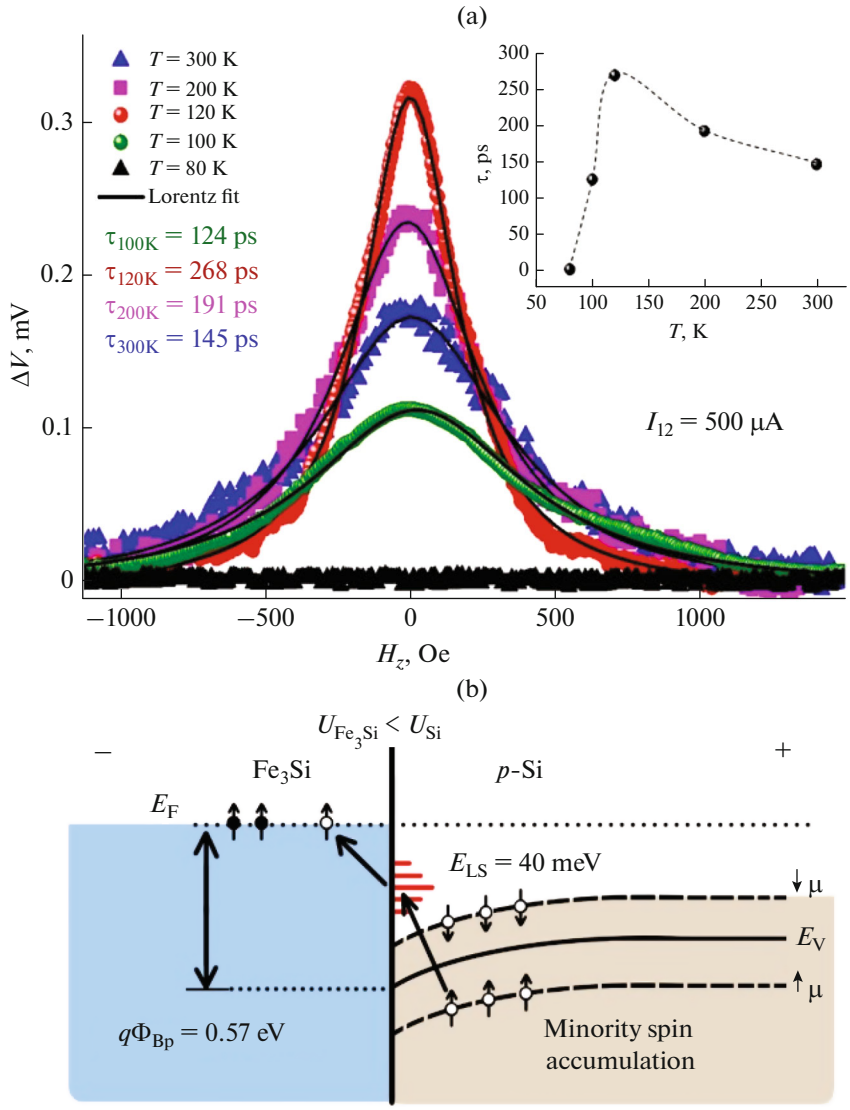

Fig. 6. (a) Hanle curves for the Fe_3Si/p-Si device at $I_{12} = +500$ μA and temperatures of 300, 200, and 120 K (symbols). Lorentz fitting is shown by black solid lines. The inset on the right shows the dependence of the spin lifetime on temperature. (b) Energy band diagram demonstrating the scheme of spin-polarized holes tunneling through the Fe_3Si/p-Si transition through localized interface states.

press the spin signal due to the "conductivity mismatch" problem. One of the transport mechanisms in our structure is thermionic emission through the Schottky barrier [34], which means the presence of a spin-dependent tunneling resistance at the interface, which removes the problem of "conductivity mismatch". However, for silicon with an impurity concentration of 10^{15} cm^{-3} the Schottky barrier width is about 700 nm, and therefore it cannot be considered a tunnel barrier. In this case, over-the-barrier charge transfer occurs; therefore, the presence of the Schottky barrier cannot be considered the main reason why the spin accumulation effect is observed.

Dankert et al. [35] reported efficient spin injection into silicon through a 736 nm wide Schottky barrier, but with an additional SiO_2 tunnel layer. The authors considered the mechanism of spin injection by means of tunneling through interface states, the model of which was proposed by them earlier. However, no attempts have been made to detect such states experimentally, for example, using optical or electrical spectroscopy techniques. Using the method of impedance spectroscopy, we detected surface states in our structure with an energy of 40 eV from the top of the silicon valence band [36]. Considering the presence of the Schottky barrier and interface states, it is possible to draw an energy band diagram of the Fe_3Si/p-Si transition and propose a scheme for the transport of spin-polarized holes, which determines the observed spin signal. During the experiment, a negative bias voltage was applied to the Fe_3Si injection contact, so that the device was in the hole extraction mode. Holes from

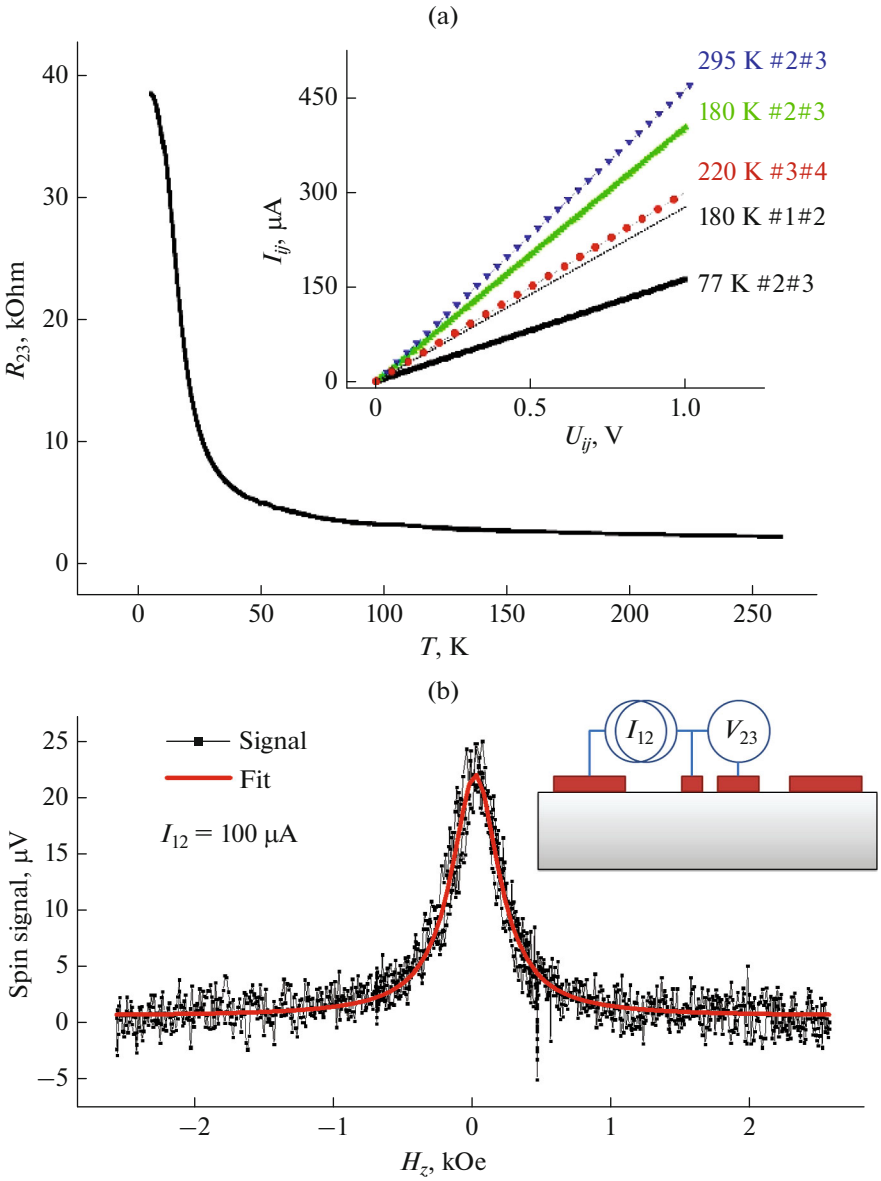

Fig. 7. (a) Resistance vs temperature curve of the Fe_3Si/n-Si microdevice measured between contacts nos. 2 and 3. The inset shows the I–V characteristics for various contacts and temperatures. (b) Spin signal ΔV observed in 3-terminal geometry at room temperature.

the valence band with the major spin direction of the Fe_3Si electrode tunnel into Fe_3Si through localized levels of surface and interface states. The probability of carrier tunneling with spin up and spin down depends on the density of states (DOS) in the corresponding subbands of the ferromagnet $D_{up}(E_F)$ and $D_{down}(E_F)$. Initially, DOS in the valence band of silicon for holes with spin up $D_{up}(E_V)$ and holes with spin down $D_{down}(E_V)$ is the same. While at the Fermi level E_F in Fe_3Si $D_{up}(E_F)$ and $D_{down}(E_F)$ is different. Therefore, hole transport from Si to Fe_3Si is spin-polarized. If Fe_3Si has a positive spin polarization, that is, if $D_{up}(E_F) - D_{down}(E_F) > 0$, then the transport channel with spin up predominates in our structure. We believe that the extraction of spin up holes results in spin accumulation of spin down holes in the silicon valence band (Fig. 6b). It should be noted that the splitting of the energy levels of the surface and interface states into spin subbands is also possible, since the same reasoning about the tunneling probability is valid for them.

Study of the electron transport was performed, the electric injection of a spin-polarized current into silicon in the Fe_3Si/n-Si epitaxial structure was demonstrated. First, the I–V characteristics between all contacts (nos. 1–4) and the corresponding temperature dependences of the resistance were measured (Fig. 7a). The I–V characteristics for all the contacts are linear (inset in Fig. 7a) in the temperature range

from 4.2 to 295 K, hence it can be concluded that the Fe_3Si/n-Si contact is ohmic. Also, the temperature dependence of the resistance measured between the contacts nos. 2 and 3 (R_{23}), is typical for silicon. This proves the absence of potential barrier between Si and Fe_3Si. The ohmic contact between the metal and low-doped silicon can be due to the formation of an intermediate $Fe_{3+x}Si_{1-x}$ layer enriched with silicon during the initial stage of film growth. It should be noted here that the synthesis conditions of Fe_3Si films on the Si(111) surface drastically affect the electrical properties of the interface.

The field dependences of local and non-local voltage ΔV were measured at a bias current $I = 100$ μA using 3-T and 4-T experimental geometry (Fig. 7b). The choice of a specific bias current value is due to the simultaneous minimization of the Joule heating of the sample and an increase in the signal-to-noise ratio of the measured voltage ΔV. In both cases, the curves fit well with the Lorentz function, which is indicative of spin accumulation in silicon. Analysis of the experimental data shows the spin lifetime $\tau(3\text{ T}) = 137$ ps and $\tau(4\text{ T}) = 134$ ps. The calculated values are comparable with other results obtained for silicon-based structures. For example, in the above-mentioned work by Fujita [32], it was reported that in the Fe_3Si/n-Si structure with a silicon doping of 6×10^{17} cm^{-3}, the lifetime value is 470 ps. In our Fe_3Si/p-Si structure, $\tau = 145$ ps. It is noteworthy that the dependence of the spin signal amplitude on the electrical displacement is observed. The measured 3-T voltage ΔV_{23} increases with an increase in the injected current I_{12}, which implies that the efficiency of spin injection depends on the electric bias [37]. At the same time, the calculated lifetime varies only within the error for different values of the current I_{12}, which was expected. In papers [38, 39] devoted to the study of structures based on highly doped silicon ($n \sim 10^{18}$ cm^{-3}) and MgO tunnel dielectric, the effect of electric bias on various spin-dependent transport data was reported, such as the efficiency of spin injection, the spin polarization of the injected current, 3-T and 4-T voltage ΔV. As in our case, there is a trend towards a decrease in the normalized spin signal and, accordingly, the efficiency of spin injection with an increase in the electric bias. It can be assumed that this trend is valid in a wide range of non-degenerate silicon impurity concentrations (10^{15}–10^{18} cm^{-3}). Comparing our results for n- and p-Si, as well as taking into account the literature data, we can conclude that the spin lifetime and the magnitude of the spin signal are affected to a greater extent by the concentration of charge carriers than by their type.

2. $Fe_{3+x}Si_{1-x}$/Ge/Fe_3Si/Si(111)

The magnetic properties of the $Fe_{3+x}Si_{1-x}$/Ge/Fe_3Si/Si(111) samples were studied. The difference in microstructure and degree of crystallinity should significantly affect the magnetic properties, including magnetization, coercive force, and anisotropy. Indeed, the saturation magnetization (Fig. 8a for the #Ge4 sample is higher by 40%. Coercive force H_c for this sample is 1.5 ± 0.2 Oe which is almost 3 times lower, while for sample #Ge7 it is 4.1 ± 0.2 Oe. In addition to significant differences in these parameters, the #Ge7 sample demonstrates some magnetization reversal features (arrows in Fig. 8a), which can be related to the presence of additional ferromagnetic phases, the formation of nonstoichiometric compositions near the interfaces, or, most likely, the crystalline imperfection of the Fe_3Si layers. Like the magnetization reversal loops, the FMR spectra differ for structures with 4 and 7 nm Ge layers. The spectra show two distinct absorption lines corresponding to two layers of $Fe_{3+x}Si_{1-x}$ ferromagnetic films (Fig. 8b). It has been established that the angular dependences of the resonance field of the FMR spectra measured in the film plane have a pronounced easy-axis anisotropy (Fig. 8c), as well as an anisotropy corresponding to the cubic crystal symmetry of Fe_3Si, which indicates the epitaxial ratio $Fe_3Si(111)\|Ge(111)\|Fe_3Si(111)\|Si(111)$. Figure 8c also shows theoretical curve calculated taking into account uniaxial, four-fold and six-fold anisotropy. One can see good agreement between the experiment and calculated data. Analyzing the FMR data, one should note the high calculated M_S value for the 1st line (1034 G for #Ge4 and 955 G for #Ge7), which is comparable to high-quality Fe_3Si epitaxial films that were grown separately on various substrates by our team and other authors [29].

Based on the synthesized structures, two-terminal planar structures were fabricated, which schematics is shown in the inset in Fig. 9a. The transport properties of the synthesized structures were studied, the temperature dependences of the resistance in Ge were measured for films with different thicknesses. Note that the contact remains ohmic up to 5 K, i.e., the I–V characteristics are linear over the entire temperature range for both samples. The resistance R of the #Ge4 sample increases non-linearly with decreasing temperature, increasing by about a factor of 3 at 5 K compared to R at 300 K (left panel in Fig. 9a). At the same time, the #Ge7 sample demonstrates a completely different behavior; upon cooling, its resistance first decreases monotonically, reaching a minimum at 55 K, and then increases (right panel in Fig. 9a). Also, the relative changes are very small, the ratio of the minimum resistance to the room temperature resistance R_{min}/R_{300} is 0.95, that is, a 5% change. Over the entire temperature range, the change is only 2.5% ($R_5/R_{300} = 0.975$). The $R(T)$ curve for the #Ge4 sample is indicative of thermally activated conduction. However, fitting in Arrhenius coordinates ($\ln(R)$ vs. $1/T$) does not give a good linear approximation. The best linearization is obtained using the expression $R =$

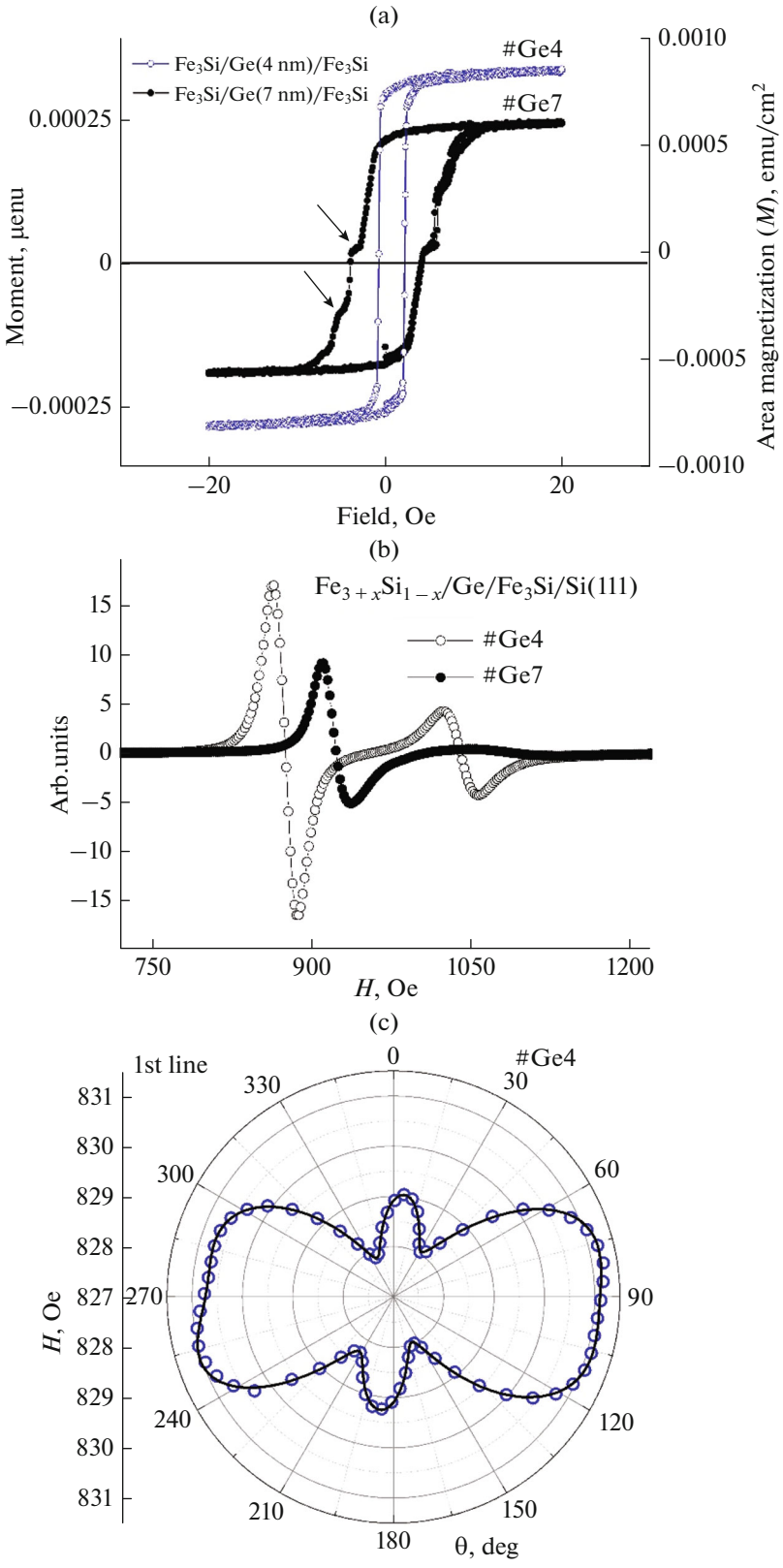

Fig. 8. (a) Magnetization reversal loops and (b) FMR spectra for the $Fe_{3+x}Si_{1-x}$/Ge(4 nm)/Fe_3Si and $Fe_{3+x}Si_{1-x}$/Ge(7 nm)/Fe_3Si structures. (c) Experimental (symbols) and calculated (line) angular dependences of the 1st line of the FMR spectrum for the $Fe_{3+x}Si_{1-x}$/Ge(4 nm)/Fe_3Si structure.

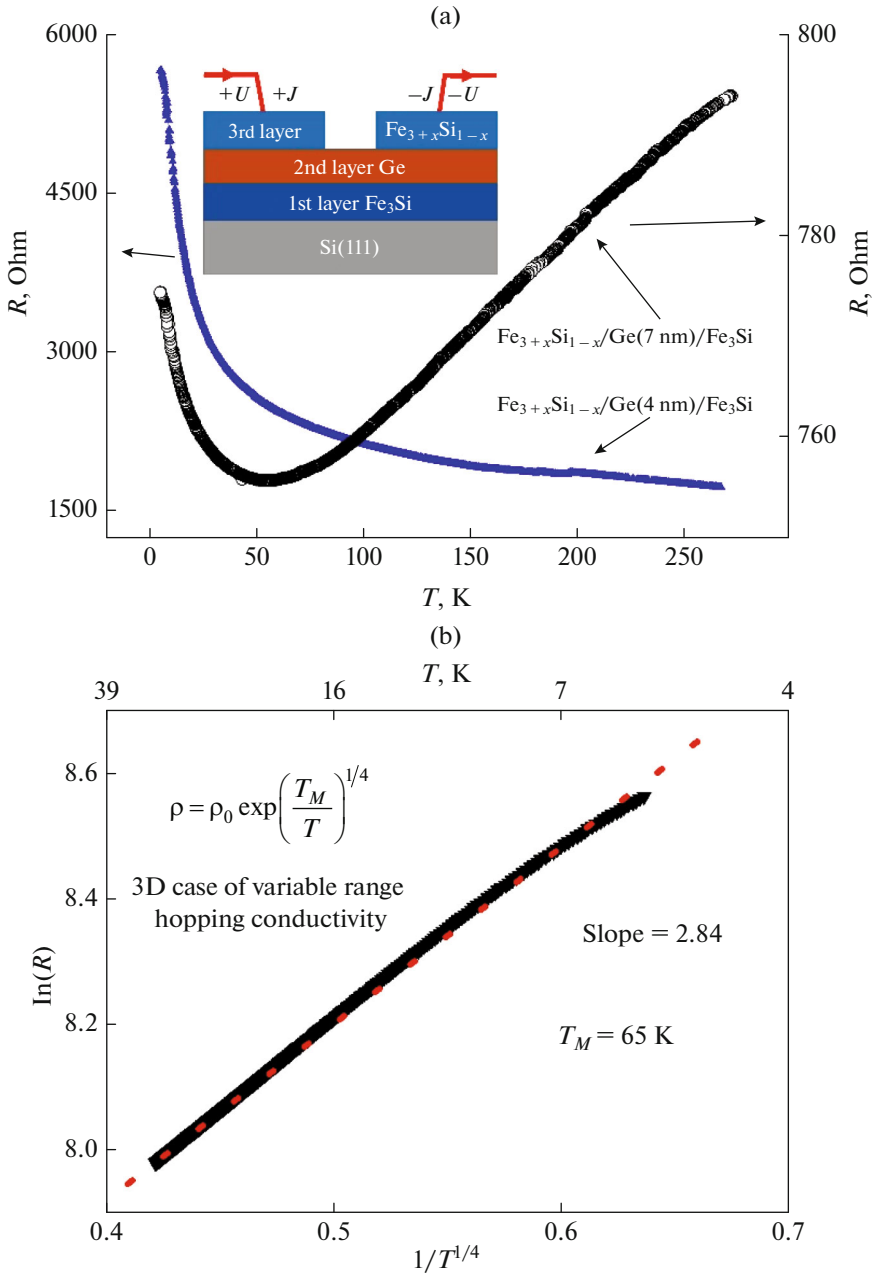

Fig. 9. (a) Temperature dependences of the resistance of $Fe_{3+x}Si_{1-x}$/Ge(4 nm)/Fe_3Si and $Fe_{3+x}Si_{1-x}$/Ge(7 nm)/Fe_3Si structures, measured in 2 contact mode. (b) Fitting of $R(T)$ curves for #Ge4 sample.

$R_0\exp(T_0/T^{1/4})$ (Fig. 9b). This suggests that the hopping type of conductivity with variable hopping length (VRH) [40] prevails over the thermal delocalization of carriers and their transfer to the conduction band of germanium. The dominance of the VRH mechanism is most likely due to the small thickness of the Ge interlayer and, accordingly, the high density of defects. Sample #Ge7 resistance is of degenerate semiconductor type. Taking into account very small changes with temperature (R_5/R_{300} = 0.975), we believe that the decrease of resistance in the temperature range from 300 to 55 K is related to an increase in the mobility of charge carriers due to a decrease in electron-phonon scattering. Low-temperature part of the curve, can't be approximated by standard functions, typical for thermally activated conductivity ($\ln(R) \sim 1/T$), the tunneling mechanism between granules in a granular system ($\ln(R) \sim 1/T^{1/2}$) [41], or VRH ($\ln(R) \sim 1/T^{1/4}$). It can be assumed that the increase in resistance below 55 K can be caused by scattering on magnetic impurities, i.e., Kondo scattering [42]. Fe impurities are most likely present at least at the Ge/Fe_3Si

interfaces. Another explanation may be related to quantum corrections to conductivity at low temperatures [43].

3. Mn_5Ge_3/Si(111) and $Fe_{3+x}Si_{1-x}$/Ge/Mn_5Ge_3/Si(111)

The magnetic properties of the Mn_5Ge_3 film and $Fe_{3+x}Si_{1-x}$/Ge/Mn_5Ge_3 structure were studied. For Mn_5Ge_3, an ordering temperature T_C of about 300 K is observed (Fig. 10a). For previously synthesized films on Ge substrates, T_C is also about 300 K [44], which is in good agreement with our samples. For bulk Mn_5Ge_3, T_C has been reported to be in the range from 296 to 304 K [45–48]. According to [49], an excess of Mn can lead to an increase in the transition temperature. While doping with silicon leads to a decrease of T_C [47], we can therefore exclude diffusion of Si from the substrate into the film. It follows that the buffer layer can be used as a diffusion barrier. The $Fe_{3+x}Si_{1-x}$/Ge/Mn_5Ge_3 structure exhibits a similar magnetization behavior, except that above T_C for Mn_5Ge_3, the magnetization is non-zero, since T_C for Fe_3Si exceeds 800 K. It should be noted that, despite the more complex technical process for obtaining Mn_5Ge_3 as part of a three-layer structure, including a longer exposure to an elevated temperature, its T_C remained unchanged, so there was neither a change in the stoichiometry of the Mn_5Ge_3 film, nor doping with iron, which would inevitably lead to an increase in T_C [48]. The shape of field dependence of the magnetization $M(H)$ (Fig. 10b) is typical of Mn_5Ge_3 films. In our case, the crystallographic c axis, which is the easy magnetization axis, is directed normally to the film surface. At the same time, a 165 nm-thick film has an easy-plane anisotropy, resulting in a specific stripe domain structure [49], which determines the shape of the loop. For the $Fe_{3+x}Si_{1-x}$/Ge/Mn_5Ge_3 structure, a low-coercivity loop from iron silicide is observed at 325 K (Fig. 10c). At low temperatures, $M(H)$ (Fig. 10c) repeats the features of the Mn_5Ge_3 film loop. Additionally, during magnetization, an inflection is observed near 300 Oe, which cannot be unambiguously associated with either silicide or germanide. It can be assumed that during synthesis at one of the $Fe_{3+x}Si_{1-x}$/Ge or Ge/Mn_5Ge_3 interfaces, parasitic ferromagnetic phase was formed, for example, Fe_xGe with T_C close to that of Mn_5Ge_3 [50].

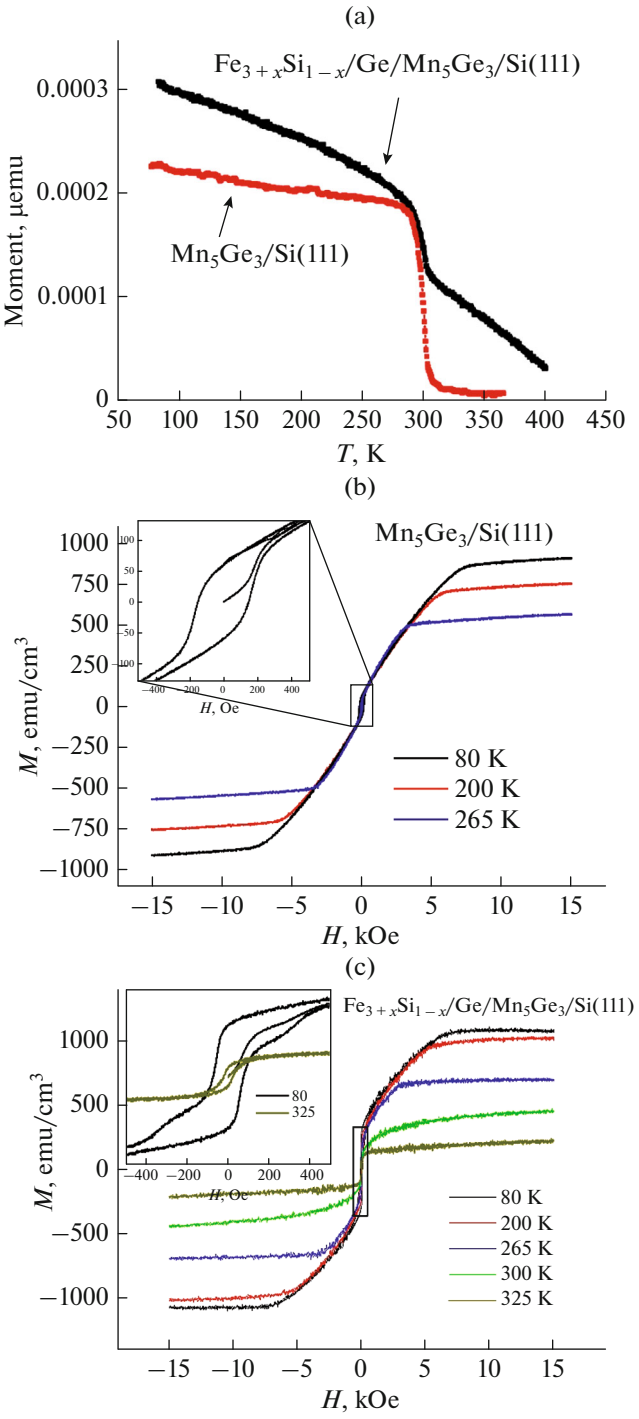

Fig. 10. (a) Temperature dependences of magnetization for Mn_5Ge_3 film and $Fe_{3+x}Si_{1-x}$/Ge/Mn_5Ge_3 structure. (b) Magnetization reversal loops for Mn_5Ge_3 and (c) $Fe_{3+x}Si_{1-x}$/Ge/Mn_5Ge_3.

For both samples, the temperature dependences of the electrical resistance were measured, which are shown in Fig. 11. As the temperature rises, the resistance increases, which is typical for metals. At temperatures around 220 K, an inflection is observed, after which the resistance begins to decrease. This effect can be due to current shunting by the substrate, which was previously observed for various films, including $Fe_{3+x}Si_{1-x}$ epitaxial films grown on Si substrates [23, 51–56]. As a result, if the substrate resistance is lower than the film resistance, then the current channel switches, i.e., the current begins to flow predominantly through the Si substrate. The temperature of switching depends on the resistance of the film,

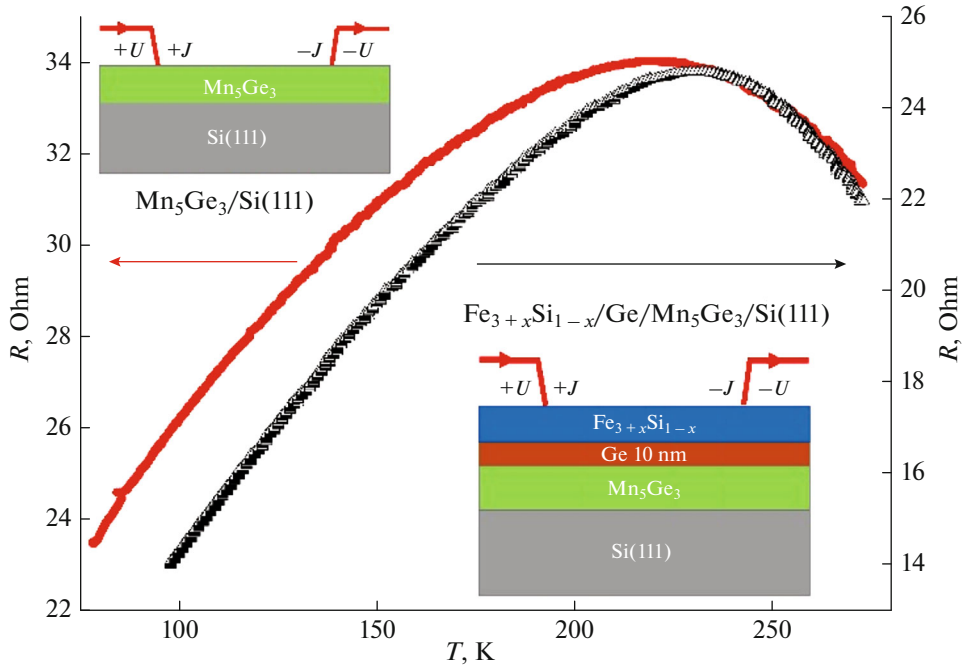

Fig. 11. Temperature dependences of electrical resistance for Mn_5Ge_3 film (left panel) and $Fe_{3+x}Si_{1-x}/Ge/Mn_5Ge_3$ structure (right panel).

which is determined by its physical properties and thickness. Based on the fact that the temperature of the peak resistance is higher for $Fe_{3+x}Si_{1-x}/Ge/Mn_5Ge_3$, we can conclude that the effective resistance of the three-layer structure is lower than that of the Mn_5Ge_3 film.

CONCLUSIONS

$Fe_3Si/p(n)$-Si hybrid structures were synthesized, planar $Fe_3Si/p(n)$-Si based devices were fabricated using the lithographic technologies. A comprehensive study of the electrical properties made it possible to propose an interpretation of the spin accumulation effect taking into account surface states in Fe_3Si/p-Si structures with a low-doped silicon substrate. Comparing the results for n- and p-Si, one can conclude that the spin lifetime and the magnitude of the spin signal are affected more by the concentration of charge carriers than by their type.

$Fe_{3+x}Si_{1-x}/Ge/Fe_3Si$ three-layer structures were grown on the Si(111) surface by molecular beam epitaxy, with Ge thicknesses of 4 and 7 nm. Systematic studies of the structural, magnetic, and transport properties of the synthesized samples have shown that an increase in Ge thickness leads to a significant change in the structural and magnetic properties of the upper $Fe_{3+x}Si_{1-x}$ layer and slight changes in the transport properties of Ge. An increase in the Ge thickness causes diffusion of atoms through the interfaces, which significantly increases the lattice mismatch in the $Ge/Fe_{3+x}Si_{1-x}$ heterosystem due to the incorporation of Ge atoms into the lower $Fe_{3+x}Si_{1-x}$ layer. It has been established that the angular dependences of the resonance field of the FMR spectra measured in the film plane have a pronounced easy axis type anisotropy, as well as an anisotropy corresponding to the cubic crystal symmetry of Fe_3Si, which indicates the epitaxial ratio $Fe_3Si(111)\|Ge(111)\|Fe_3Si(111)\|Si(111)$. The temperature dependences of the electrical resistance of 4 nm- and 7 nm-germanium layers have a semiconductor type, but are determined by different transport mechanisms, which is probably associated with different concentrations of defects.

Using the buffer layer approach, Mn_5Ge_3 epitaxial films were grown on Si(111). $Fe_{3+x}Si_{1-x}/Ge/Mn_5Ge_3/Si(111)$ structures were synthesized using the technology of three-layer structures growth. Magnetic characterization revealed that $T_C = 300$ K corresponds to bulk Mn_5Ge_3 and to films grown on Ge and GaAs. Moreover, the T_C values for the film and the three-layer structure are the same, which rules out the Mn_5Ge_3 doping with silicon, germanium, or iron during diffusion from other layers. For $Fe_{3+x}Si_{1-x}/Ge/Mn_5Ge_3$ above 300 K, there is clearly a low coercive signal from ferromagnetic iron silicide, which, along with the RHEED data, indicates a good quality of the upper film. The temperature dependences of the resistance for $Mn_5Ge_3/Si(111)$ and $Fe_{3+x}Si_{1-x}/Ge/Mn_5Ge_3/Si(111)$ demonstrate similar behavior, exhibiting the effect of current channel switching above 200 K. We believe that the discovered relation and features of the structural, magnetic, and transport properties of hybrid

structures based on ferromagnetic silicides and germanides will expand the methods for obtaining magnetic epitaxial films and structures. Additionally, these findings hold potential for advancing the field of spintronics.

ACKNOWLEDGMENTS

The authors thank the laboratory of Magnetic MAX Materials created under Megagrant project (agreement no. 075-15-2019-1886) for providing experimental equipment and the Collective Use Center at the Krasnoyarsk Scientific Center (Siberian Branch, Russian Academy of Sciences) for assistance. The authors also thank Professor B.A. Belyaev for FMR calculations.

FUNDING

Supported by the Russian Science Foundation, grant no. 23-22-10033, https://rscf.ru/project/23-22-10033/, Krasnoyarsk Regional Fund of Science.

CONFLICT OF INTEREST

The authors declare that they have no conflicts of interest.

REFERENCES

1. Zutic, I., Fabian, J., and Das Sarma, S., *Rev. Mod. Phys.*, 2004, vol. 76, no. 2, p. 323. https://doi.org/10.1103/RevModPhys.76.323
2. Jansen, R., *Nat. Mater.*, 2012, vol. 11, p. 400–408. https://doi.org/10.1038/NMAT3293
3. Hirohata, A., Yamada, K., Nakatani, Y., Prejbeanu, I.L., Diény, B., Pirro, P., and Hillebarnds, B., *J. Magn. Magn. Mater.*, 2020, vol. 509, p. 166711. https://doi.org/10.1016/j.jmmm.2020.166711
4. Volkov, N., *Phys—Usp.*, 2012, vol. 55, p. 250. https://doi.org/10.3367/UFNe.0182.201203b.0263
5. Baranov, P.G., Kalashnikova, A.M., Kozub, V.I., Korenev, V.L., Kusrayev, Y.G., Pisarev, R.V., Sapega, V.F., Akimov, I.Y., Bayer, M., Scherbakov, A.V., and Yakovlev, D.R., *Phys.—Usp.*, 2019, vol. 62, p. 795. https://doi.org/10.3367/UFNe.2018.11.038486
6. Wollmann, L., Nayak, A.K., Parkin, S.S., and Felser, C., *Annu. Rev. Mater. Res.*, 2017, vol. 47, p. 247. https://doi.org/10.1146/annurev-matsci-070616-123928
7. Baigutlin, D.R., Sokolovskiy, V.V., Miroshkina, O.N., and Buchelnikov, V.D., *Fiz. Tverd. Tela*, 2021, vol. 63, no. 11, p. 1751. https://doi.org/10.21883/FTT.2021.11.51572.18s
8. Prudnikov, V.N., Kazakov, A.P., Titov, I.S., Perov, N.S., Granovskii, A.B., Dubenko, I.S., Pathak, A.K., Ali, N., Zhukov, A.P., and Gonzalez, J., *JETP Lett.*, 2015, vol. 119, p. 969. https://doi.org/10.1134/S0021364010220066
9. Shreder, E.I., Svyazhin, A.D., and Makhnev, A.A., *Opt. Spectrosc.*, 2015, vol. 119, p. 969. https://doi.org/10.1134/S0030400X1511020X
10. Eremeev, S.V., S.E. Kul'Kova, and S.S. Kul'kov, *Phys. Solid State*, 2008, vol. 50, p. 259. https://doi.org/10.1134/S106378340802008X
11. Granovskii, A.B., Prudnikov, V.N., Kazakov, A.P., Zhukov, A.P., and Dubenko, I.S., *J. Exp. Theor. Phys.*, 2012, vol. 115, p. 805. https://doi.org/10.1134/S1063776112090051
12. Demidov, E.S., Karzanov, V.V., Sapozhnikov, M.V., Gusev, S.N., Levchuk, S.A., Podolskii, V.V., Lesnikov, V.P., Aronzon, B.A., and Rylkov, V.V., *Bull. Russ. Acad. Sci.: Phys.*, 2010, vol. 74, p. 1389. https://doi.org/10.3103/S1062873810100187
13. Gaidukova, I.Y., Granovskiy, S.A., and Markosyan, A.S., *Bull. Russ. Acad. Sci.: Phys.*, 2010, vol. 74, p. 1373. https://doi.org/10.3103/S1062873810100138
14. Hamaya, K., Fujita, Y., Yamada, M., Kawano, M., Yamada, S., and Sawano, K., *J. Phys. D: Appl. Phys.*, 2018, vol. 51, no. 39, p. 393001. https://doi.org/10.1088/1361-6463/aad542
15. Ovchinnikov, S.G., Varnakov, S.N., Lyashchenko, S.A., Tarasov, I.A., Yakovlev, I.A., Popov, E.A., Zharkov, S.M., Velikanov, D.A., Tarasov, A.S., Zhandun, V.S., and Zamkova, N.G., *Phys. Solid State*, 2016, vol. 58, p. 2277. https://doi.org/10.1134/S1063783416110299
16. Tarasov, A.S., Lukyanenko, A.V., Bondarev, I.A., Rautskii, M.V., Baron, F.A., Smolyarova, T.E., Yakovlev, I.A., Varnakov, S.N., Ovchinnikov, S.G., and Volkov, N.V., *Semiconductors*, 2018, vol. 52, no. 14, p. 1875. https://doi.org/10.1134/S1063782618140312
17. Lukyanenko, A.V., Tarasov, A.S., Shanidze, L.V., Volochaev, M.N., Zelenov, F.V., Yakovlev, I.A., Bondarev, I.A., and Volkov, N.V., *J. Surf. Invest.: X-ray, Synchrotron Neutron Tech.*, 2021, vol. 15, no. 1, p. 65. https://doi.org/10.1134/S1027451021010109
18. Smolyakov, D.A., Tarasov, A.S., Yakovlev, I.A., and Volochaev, M.N., *Semiconductors*, 2019, vol. 53, no. 14, p. 98. https://doi.org/10.1134/S1063782619140215
19. Smolyakov, D.A., Rautskii, M.V., Bondarev, I.A., Yakovlev, I.A., Ovchinnikov, S.G., Volkov, N.V., and Tarasov, A.S., *J. Exp. Theor. Phys.*, 2022, vol. 135, p. 377. https://doi.org/10.1134/S1063776122090102
20. Volkov, N.V., Tarasov, A.S., Rautskii, M.V., Lukyanenko, A.V., Baron, F.A., Bondarev, I.A., Varnakov, S.N., and Ovchinnikov, S.G., *J. Exp. Theor. Phys.*, 2015, vol. 9, no. 5, p. 984. https://doi.org/10.1134/S1027451015050432
21. Bondarev, I.A., Rautskii, M.V., Yakovlev, I.A., Volochaev, M.N., Lukyanenko, A.V., Tarasov, A.S., and Volkov, N.V., *Semiconductors*, 2019, vol. 53, no. 14, p. 88.
22. Yakovlev, I.A., Tarasov, I.A., and Lyashchenko, S.A., *J. Magn. Magn. Mater.* 2017, vol. 440, p. 161. https://doi.org/10.1016/j.jmmm.2016.12.051
23. Tarasov, A.S., Lukyanenko, A.V., Tarasov, I.A., Bondarev, I.A., Smolyarova, T.E., Kosyrev, N.N., Komarov, V.A., Yakovlev, I.A., Volochaev, M.N., Solovyov, L.A., Shemukhin, A.A., Varnakov, S.N., Ovchinnikov, S.G., Patrin, G.S., and Volkov, N.V., *Thin Solid Films*, 2017, vol. 642, p. 20. https://doi.org/10.1016/j.tsf.2017.09.025

24. Volkov, N.V., Tarasov, A.S., Rautskii, M.V., Lukyanenko, A.V., Bondarev, I.A., Varnakov, S.N., and Ovchinnikov, S.G., *J. Magn. Magn. Mater.*, 2018, vol. 451, p. 143. https://doi.org/10.1016/j.jmmm.2017.11.008
25. Tarasov, A.S., Tarasov, I.A., Yakovlev, I.A., Rautskii, M.V., Bondarev, I.A., Lukyanenko, A.V., Platunov, M.S., Volochaev, M.N., Efimov, D.D., Goikhman, A.Y., Belyaev, B.A., Baron, F.A., Shanidze, L.V.,; Farle, M., Varnakov, S.N., Ovchinnikov, S.G., and Volkov, N.V., *Nanomaterials*, 2022, vol. 12, p. 131. https://doi.org/10.3390/nano12010131
26. Petit, M., Boussadi, A., Heresanu, V., Ranguis, A., and Michez, L., *Appl. Surf. Sci.*, 2019, vol. 480, p. 529. https://doi.org/10.1016/j.apsusc.2019.01.164
27. Hamaya, K., Ando, Y., Sadoh, T., and Miyao, M., *Jpn. J. Appl. Phys.*, 2011, vol. 50, no. 1R, p. 010101. https://doi.org/10.1143/JJAP.50.010101
28. Lenz, K., Kosubek, E., Baberschke, K., Wende, H., Herfort, J., Schönherr, H.P., and Ploog, K.H., *Phys. Rev. B*, 2005, vol. 72, no. 14, p. 144411. https://doi.org/10.1103/PhysRevB.72.144411
29. Zakeri, Kh., Lindner, J., Barsukov, I., Meckenstock, R., Farle, M., von Hörsten, U., Wende, H., Keune, W., Rocker, J., Kalarickal, S.S., Lenz, K., Kuch, W., Baberschke, K., and Frait, Z., *Phys. Rev. B*, 2007, vol. 76, no. 10, p. 104416. https://doi.org/10.1103/PhysRevB.76.104416
30. Spiesser, A., Sharma, S., Saito, H., Jansen, R., Yuasa, S., and Ando, K., *Proc. SPIE*, 2012, vol. 8461, p. 84610K. https://doi.org/10.1117/12.930839
31. Dash, S.P., Sharma, S., Le Breton, J.C., Peiro, J., Jaffrès, H., George, J.-M., Lemaître, A., and Jansen, R., *Phys. Rev. B*, 2011, vol. 84, 054410. https://doi.org/10.1103/PhysRevB.84.054410
32. Fujita, Y., Yamada, S., Ando, Y., Sawano, K., Itoh, H., Miyao, M., and Hamaya, K., *J. Appl. Phys.*, 2013, vol. 113, no. 1, p. 013916. https://doi.org/10.1063/1.4773072
33. Fert, A. and Jaffres, H., *Phys. Rev. B*, 2001, vol. 64, no. 18, p. 184420. https://doi.org/10.1103/PhysRevB.64.184420
34. Tarasov, A.S., Bondarev, I.A., Rautskii, M.V., Lukyanenko, A.V., Tarasov, I.A., Varnakov, S.N., Ovchinnikov, S.G., and Volkov, N.V., *J. Surf. Invest.: X-ray, Synchrotron Neutron Tech.*, 2018, vol. 12, no. 4, p. 633. https://doi.org/10.1134/S1027451018040171
35. Dankert, A., Dulal, R.S., and Dash, S.P., *Sci. Rep.*, 2013, vol. 3, p. 3196. https://doi.org/10.1038/srep03196
36. Tarasov, A.S., Lukyanenko, A.V., Rautskii, M.V., Bondarev, I.A., Smolyakov, D.A., Tarasov, I.A., Yakovlev, I.A., Varnakov, S.N., Ovchinnikov, S.G., Baron, F.A., and Volkov, N.V., *Semicond. Sci. Technol.*, 2019, vol. 34, p. 035024. https://doi.org/10.1088/1361-6641/ab0327
37. Tarasov, A.S., Lukyanenko, A.V., Bondarev, I.A., Yakovlev, I.A., Varnakov, S.N., Ovchinnikov, S.G., and Volkov, N.V., *Tech. Phys. Lett.*, 2020, vol.46, p. 665. https://doi.org/10.1134/S1063785020070135
38. Lee, S., Rortais, F., Ohshima, R., Ando, Y., Miwa, S., Suzuki, Y., Koike, H., and Shiraishi, M., *Phys. Rev. B*, 2019, vol. 99, p. 064408. https://doi.org/10.1103/PhysRevB.99.064408
39. Spiesser, A., Fujita, Y., Saito, H., Yamada, S., Hamaya, K., Mizubayashi, W., Endo, K., Yuasa, S., and Jansen, R., *Phys. Rev. Appl.*, 2019, vol. 11, p. 044020. https://doi.org/10.1103/PhysRevApplied.11.044020
40. Mott, N.F. and Davis, E.A., *Electronic Processes in Noncrystalline Materials*, Oxford: Oxford Univ. Press, 2012.
41. Sheng, P., Abeles, B., and Arie, Y., *Phys. Rev. Lett.*, 1973, vol. 31, p. 44. https://doi.org/10.1103/PhysRevLett.31.44
42. Kittle, C., *Introduction to Solid State Physics*, New York: Wiley, 2009, p. 628.
43. Lee, P.A. and Ramakrishnan, T.V., *Rev. Mod. Phys.*, 1985, vol. 57, p. 287. https://doi.org/10.1103/RevModPhys.57.287
44. Bechler, S., Kern, M., Funk, H.S., Colston, G., Fischer, I.A., Weißhaupt, D., Myronov, M., Slageren, J., and Schulze, J., *Semicond. Sci. Technol.*, 2018, vol. 33, no. 9, p. 095008. https://doi.org/10.1088/1361-6641/aad4cf
45. Zheng, T.F., Shi, Y.G., Hu, C.C., Fan, J.Y., Shi, D.N., Tang, S.L., and Du, Y.W., *J. Magn. Magn. Mater.*, 2012, vol. 324, no. 23, p. 4102. https://doi.org/10.1016/j.jmmm.2012.07.031
46. Songlina, Dagula, W., Tegus, O., Brück, E., de Boer, F.R., Buschow, K.H.J., *J. Alloys Compd.*, 2002, vol. 337, nos. 1–2, p. 269. https://doi.org/10.1016/S0925-8388(01)01935-1
47. Zhao, F.Q., Dagula, W., Tegus, O., and Buschow, K.H.J., *J. Alloys Compd.*, 2006, vol. 416, nos. 1–2, p. 43. https://doi.org/10.1016/j.jallcom.2005.08.039
48. Kim, Y., Kang, K.H., Kim, J.H., Kim, E.J., Choi, K., Han, W.B., Kim, H.S., Oh, Y., and Yoon, C.S., *J. Alloys Compd.*, 2015, vol. 644, p. 464. https://doi.org/10.1016/j.jallcom.2015.05.061
49. Michez, L.A., Spiesser, A., Petit, M., Bertaina, S., Jacquot, J.F., Dufeu, D., Coudreau, C., Jamet, M., and Le Thanh, V., *J. Phys.: Condens. Matter*, 2015, vol. 27, no. 9, p. 266001. http://iopscience.iop.org/0953-8984/27/26/266001.
50. Yasukojchi, K. and Kanematsu, K., *J. Phys. Soc. Jpn.*, 1961, vol. 16, no. 3, p. 429. https://doi.org/10.1143/JPSJ.16.429
51. Volkov, N.V., Tarasov, A.S., Eremin, E.V., Varnakov, S.N., Ovchinnikov, S.G., and Zharkov, S.M., *J. Appl. Phys.*, 2011, vol. 109, p. 123924. https://doi.org/10.1063/1.3600056
52. Volkov, N.V., Eremin, E.V., Tarasov, A.S., Rautskii, M.V., Varnakov, S.N., Ovchinnikov, S.G., and Patrin, G.S., *J. Magn. Magn. Mater.*, 2012, vol. 324, p. 3579. https://doi.org/10.1016/j.jmmm.2012.02.095
53. Volkov, N.V., Eremin, E.V., Tarasov, A.S., Varnakov, S.N., and Ovchinnikov, S.G., *Solid State Phenom.*, 2012, vol. 190, p. 526. https://doi.org/10.4028/www.scientific.net/SSP.190.526
54. Vikulov, V.A., Dimitriev, A.A., Balashev, V.V., Pisarenko, T.A., and Korobtsov, V.V., *Mater. Sci. Eng., B.*, 2016, vol. 211, p. 33. https://doi.org/10.1016/j.mseb.2016.05.014